

## Rutile alloys in the Mn-Sb-O system stabilize Mn +3 to enable oxygen evolution in strong acid

Lan Zhou, Aniketa Shinde, Joseph H. Montoya, Arunima Singh, Sheraz Gul, Junko Yano, Yifan Ye, Ethan J. Crumlin, Matthias H. Richter, Jason K. Cooper, Helge Stein, Joel A. Haber, Kristin Persson, and John M. Gregoire

*ACS Catal.*, **Just Accepted Manuscript** • Publication Date (Web): 16 Oct 2018

Downloaded from <http://pubs.acs.org> on October 16, 2018

### Just Accepted

“Just Accepted” manuscripts have been peer-reviewed and accepted for publication. They are posted online prior to technical editing, formatting for publication and author proofing. The American Chemical Society provides “Just Accepted” as a service to the research community to expedite the dissemination of scientific material as soon as possible after acceptance. “Just Accepted” manuscripts appear in full in PDF format accompanied by an HTML abstract. “Just Accepted” manuscripts have been fully peer reviewed, but should not be considered the official version of record. They are citable by the Digital Object Identifier (DOI®). “Just Accepted” is an optional service offered to authors. Therefore, the “Just Accepted” Web site may not include all articles that will be published in the journal. After a manuscript is technically edited and formatted, it will be removed from the “Just Accepted” Web site and published as an ASAP article. Note that technical editing may introduce minor changes to the manuscript text and/or graphics which could affect content, and all legal disclaimers and ethical guidelines that apply to the journal pertain. ACS cannot be held responsible for errors or consequences arising from the use of information contained in these “Just Accepted” manuscripts.

# Rutile Alloys in the Mn-Sb-O System Stabilize Mn<sup>+3</sup> to Enable Oxygen Evolution in Strong Acid

Lan Zhou<sup>1</sup>, Aniketa Shinde<sup>1</sup>, Joseph H. Montoya<sup>2</sup>, Arunima Singh<sup>3,4</sup>, Sheraz Gul<sup>5</sup>, Junko Yano<sup>3,5</sup>, Yifan Ye<sup>3,4,6</sup>, Ethan J. Crumlin<sup>6</sup>, Matthias H. Richter<sup>1,7</sup>, Jason K. Cooper<sup>3,4</sup>, Helge S. Stein<sup>1</sup>, Joel A. Haber<sup>1</sup>, Kristin A. Persson<sup>2,3,8,\*</sup>, John M. Gregoire<sup>1,\*</sup>

<sup>1</sup> Joint Center for Artificial Photosynthesis, California Institute of Technology, Pasadena, CA 91125, USA.

<sup>2</sup> Environmental Energy Technologies Division, Lawrence Berkeley National Laboratory, Berkeley, CA 94720, USA.

<sup>3</sup> Joint Center for Artificial Photosynthesis, Lawrence Berkeley National Laboratory, Berkeley, CA 94720, USA.

<sup>4</sup> Chemical Sciences Division, Lawrence Berkeley National Laboratory, Berkeley, CA 94720, USA

<sup>5</sup> Molecular Biophysics and Integrated Bioimaging Division, Lawrence Berkeley National Laboratory, Berkeley, CA 94720, USA.

<sup>6</sup> Advanced Light Source, Lawrence Berkeley National Laboratory, One Cyclotron Road, Berkeley, California 94720, USA

<sup>7</sup> Division of Chemistry and Chemical Engineering, California Institute of Technology, Pasadena, CA 91125, USA

<sup>8</sup> Department of Materials Science and Engineering, University of California, Berkeley, CA 94720, USA.

\*Correspondence to: Kristin A. Persson (kapersson@lbl.gov), John M. Gregoire (gregoire@caltech.edu)

## ABSTRACT:

Electrocatalysis of the oxygen evolution reaction is central to several energy technologies including electrolyzers, solar fuel generators, and air-breathing batteries. Strong acid electrolytes are desirable for many implementations of these technologies, although the deployment of such device designs is often hampered by the lack of non-precious metal oxygen evolution electrocatalysts, with Ir-based oxides comprising the only known catalysts that exhibit stable activity at low overpotential. During our exploration of the Mn-Sb-O system for precious-metal-

1  
2  
3 free electrocatalysts, we discovered that Mn can be incorporated into the rutile oxide structure at  
4 much higher concentrations than previously known, and that these Mn-rich rutile alloys exhibit  
5 great catalytic activity with current densities exceeding  $50 \text{ mA cm}^{-2}$  at 0.58 V overpotential and  
6 catalysis onset at 0.3 V overpotential. While this activity does not surpass that of  $\text{IrO}_2$ , Pourbaix  
7 analysis reveals that the Mn-Sb rutile oxide alloys have the same or better thermodynamic  
8 stability under operational conditions. By combining combinatorial composition, structure, and  
9 activity mapping with synchrotron x-ray absorption measurements and first-principles materials  
10 chemistry calculations, we provide a comprehensive understanding of these oxide alloys and  
11 identify the critical role of Sb in stabilizing the tri-valent Mn octahedra that have been shown to  
12 be effective OER catalysts.  
13  
14  
15  
16  
17  
18  
19  
20  
21  
22  
23  
24  
25

26  
27 Keywords:

28  
29 oxygen evolution reaction, catalysis, electrochemical stability, metal oxide alloys, combinatorial  
30 materials science  
31  
32  
33  
34  
35  
36

## 37 1. INTRODUCTION

38  
39  
40 The development of active, stable, and earth-abundant oxygen evolution catalysts in acid  
41 environments has drawn great interest in materials chemistry research and for technological  
42 applications such as metal winning and renewable solar fuel synthesis.<sup>1</sup> Solar fuel generators  
43 that use renewable energy to photoelectrochemically synthesize fuel couple the oxygen evolution  
44 reaction (OER) to a fuel-forming reaction, typically hydrogen evolution or carbon dioxide  
45 reduction. The OER half reaction requires 4 coupled electron and proton transfers, resulting in  
46 sluggish kinetics and consequently a large overpotential; therefore, a highly active catalyst is  
47  
48  
49  
50  
51  
52  
53  
54  
55  
56  
57  
58  
59  
60

1  
2  
3 important to maximize the energy conversion efficiency.<sup>2</sup> While cost-effective, earth-abundant,  
4 efficient, and robust OER catalysts have been found for alkaline or neutral media applications,<sup>3</sup>  
5 modeling and experimental demonstrations have shown that an acidic environment is more  
6 desirable for high efficiency fuel-forming devices.<sup>4</sup> The only established acid-stable OER  
7 catalysts are based on noble metal oxides such as IrO<sub>x</sub> and RuO<sub>x</sub> that simultaneously exhibit high  
8 catalytic activity and stability in the corrosive acid environment.<sup>1</sup>  
9

10  
11  
12  
13  
14  
15  
16  
17  
18 Discovering and developing acid-stable, earth-abundant OER catalysts that achieve useful rates  
19 of oxygen evolution has proven to be very challenging, especially for low overpotential  
20 operation. Significant materials research efforts to meet this challenge include: (1) mixing noble  
21 metals (Ir, Ru) with non-noble metals (W,<sup>5</sup> Sn,<sup>6</sup> Sn-Sb,<sup>7</sup> Sn-Nb,<sup>8</sup> Mn,<sup>9</sup> Ti,<sup>10</sup> Ta,<sup>11</sup> Ni,<sup>12</sup> Co<sup>13</sup>) to  
22 achieve acid-stable, high activity with minimal noble metal content; (2) exploring noble-metal-free  
23 transition metal oxides: Co-based,<sup>14</sup> Fe-based,<sup>15</sup> and Mn-based;<sup>16</sup> and (3) designing high-order  
24 multi-cation metal oxides combining the activity of one or more metal oxides with the acid  
25 stability of other metal oxides to produce a new earth-abundant material displaying active, acid-  
26 stable OER catalysis.<sup>16</sup>  
27  
28  
29  
30  
31  
32  
33  
34  
35  
36  
37  
38

39  
40 MnO<sub>x</sub>-based catalysts are among the most studied non-noble metal OER catalysts due to  
41 inspiration from the CaMn<sub>4</sub>O cluster in the photosynthetic oxygen evolution center (OEC) and  
42 efficacy of Mn-based catalysts across a broad range of reactions, which is related to the large  
43 number of accessible oxidation states and the ensuing diverse oxide stoichiometries and  
44 polymorphs of MnO<sub>x</sub>.<sup>17</sup> The presence of Mn<sup>3+</sup> in heterogeneous catalysts is correlated with OER  
45 activity, which has limited the activity of MnO<sub>x</sub>-based OER catalysts in neutral to acidic  
46 conditions as Mn<sup>3+</sup> disproportionates to Mn<sup>2+</sup> and Mn<sup>4+</sup> at pH < 9.<sup>18</sup> The recognition of the  
47 critical role played by Mn<sup>3+</sup> in OER catalysis has led to efforts to stabilize this oxidation state in  
48  
49  
50  
51  
52  
53  
54  
55  
56  
57  
58  
59  
60

1  
2  
3 neutral and acidic pH electrolytes.<sup>19</sup> Of particular note for OER under acidic conditions is the  
4 stability and moderate activity of electrochemically activated manganese oxide; under specific  
5 deposition conditions, a cathodically treated or cyclic voltammetry (CV) deposited  $\text{MnO}_x$  film is  
6 proficient for the OER due to generation of  $\text{Mn}^{3+}$  on the surface of the  $\text{Mn}^{4+}\text{O}_2$  electrode.<sup>20</sup> This  
7 catalyst preparation proceeds by the *in situ* comproportionation of  $\text{Mn}^{4+}$  with  $\text{Mn}^{2+}$  to produce  
8 metastable, OER-active  $\text{Mn}^{3+}$  ions trapped in tetrahedral coordination sites within the  $\text{MnO}_2$   
9 matrix, which are protected from both dissolution and disproportionation under OER  
10 conditions.<sup>21</sup> At relatively low overpotentials producing relatively low current densities of 0.1  
11  $\text{mA cm}^{-2}$ , this electrochemically activated manganese oxide exhibits stable operation in acid (pH  
12 0.3 to 3), but application of higher overpotentials to increase the current density leads to  
13 manganese oxidation and film dissolution as permanganates,<sup>20c</sup> motivating exploration of  
14 materials strategies for stabilizing  $\text{MnO}_x$  at OER potentials in strong acid, which is the focus of  
15 the present work.  
16  
17  
18  
19  
20  
21  
22  
23  
24  
25  
26  
27  
28  
29  
30  
31  
32  
33

34 Among these materials-based approaches to Mn stabilization is our previous exploration of  
35 stabilizing Co and Mn active sites with multi-cation oxides in the  $(\text{Co-Mn-Ta-Sb})\text{O}_x$  system,  
36 which includes the compositions presented in this work but without control or characterization of  
37 the crystal structure, which we show here to be critical to both activity and stability.<sup>16a</sup> Huynh, M  
38 *et.al.* reported  $\text{CoMnO}_x$ <sup>16b</sup> (where XPS shows Mn is  $\text{Mn}^{4+}$ , which is relatively inactive for OER)  
39 could be operated stably at low overpotential and current density and suffered from corrosion  
40 due to the insufficient stability of both Co and Mn cations. Patel *et.al.* reported cubic structure of  
41 F-doped  $\text{Cu}_{1.5}\text{Mn}_{1.5}\text{O}_4$  nanoparticles containing both  $\text{Mn}^{3+}$  and  $\text{Mn}^{4+}$ , where the high catalytic  
42 activity was attributed to the high oxidation potential of the F anions.<sup>16c</sup> Recently, crystalline  
43 nickel-manganese antimonates with a rutile-type structure were reported in 1.0 M  $\text{H}_2\text{SO}_4$  with  
44  
45  
46  
47  
48  
49  
50  
51  
52  
53  
54  
55  
56  
57  
58  
59  
60

1  
2  
3 overpotential at  $10 \text{ mA cm}^{-2}$  increasing from  $672 \pm 9 \text{ mV}$  to  $735 \pm 10 \text{ mV}$  over 168 h of continuous  
4  
5 operation.<sup>16d, 22</sup> In the present work, we return the focus to the Mn-Sb pseudo-binary system using  
6  
7 combinatorial methods, which have been previously deployed for exploring OER catalysts in acid,<sup>23</sup>  
8  
9 to explore the relationship between physical properties and OER electrocatalytic activities of sputter-  
10  
11 deposited composition-spread thin films. We combine combinatorial synthesis and electrochemistry  
12  
13 with a range of structural, spectroscopic, and computational characterization to discover Mn-rich rutile  
14  
15 alloys of the type  $(\text{Mn}_x\text{Sb}_{1-x})\text{O}_2$  with  $x > 0.5$ , quantify the stabilization of Mn provided by the Sb-  
16  
17 based rutile oxide structure, and reveal alloying-based tuning of the Mn oxidation state and the  
18  
19 covalency of Mn-O bonds that leads to high OER activity at Mn-rich compositions.  
20  
21  
22  
23  
24

## 25 2. EXPERIMENTAL SECTION

### 26 2.1 PVD library synthesis

27  
28  
29  
30  
31 The Mn-Sb binary oxide composition libraries  $\text{Mn}_x\text{Sb}_{1-x}\text{O}_2$  were fabricated using reactive radio  
32  
33 frequency magnetron co-sputtering of Mn and Sb metal targets onto 100 mm-diameter  
34  
35 Pt/Ti/SiO<sub>2</sub>/Si substrates in a sputter deposition system<sup>24</sup> (Kurt J. Lesker, CMS24) with  $10^{-5}$  Pa  
36  
37 base pressure. The thermally grown SiO<sub>2</sub> served as a diffusion barrier, the Ti served as an  
38  
39 adhesion layer, and the Pt served as a common back contact for the composition library. The Mn-  
40  
41 Sb oxide thin films were deposited under 0.80 Pa working atmosphere composed of inert  
42  
43 sputtering gas Ar (0.72 Pa) and reactive gas O<sub>2</sub> (0.08 Pa). The composition gradients in the co-  
44  
45 sputtered continuous composition spreads were attained by positioning the deposition sources in  
46  
47 a non-confocal geometry. The deposition proceeded for 1 hour with the power on the Sb and Mn  
48  
49 source at 24 and 146 W, respectively. The as-deposited composition library was cut into 3 pieces  
50  
51 with similar composition gradient; the center strip was subsequently placed flat on a quartz  
52  
53  
54  
55  
56  
57  
58  
59  
60

1  
2  
3 support and annealed in air in a programmable Thermo Scientific box oven at 700 °C for 3  
4  
5 hours. The annealing was preceded by a 2 hour temperature ramp and was followed by natural  
6  
7 cooling. The bottom strip was annealed similarly at 550 °C for 10 hours. A second deposition  
8  
9 proceeded with a higher O<sub>2</sub> partial pressure of 0.16 Pa (total pressure of 0.8 Pa kept the same) in  
10  
11 the sputter gas to provide a higher oxygen concentration in the as-deposited film since no post-  
12  
13 deposition thermal processing was applied to this composition library.  
14  
15  
16  
17

## 18 2.2 OER catalytic measurements

19

20  
21 The OER performance of the Mn<sub>x</sub>Sb<sub>1-x</sub>O<sub>z</sub> catalysts was evaluated using a previously reported  
22  
23 scanning droplet cell (SDC)<sup>25</sup> with flowing O<sub>2</sub>-saturated 1.0 M H<sub>2</sub>SO<sub>4</sub> (aq) electrolyte solution  
24  
25 (pH=0.13). The 3-electrode cell includes a Pt counter electrode, Ag/AgCl reference electrode,  
26  
27 Gamry G 300 potentiostat, and custom LabVIEW software. The SDC moved along the binary  
28  
29 composition library and performed an experiment every 3 mm. The activity of each Mn<sub>x</sub>Sb<sub>1-x</sub>O<sub>z</sub>  
30  
31 composition was characterized using cyclic voltammetry (CV) measurements from 1.24 to 1.79  
32  
33 V and back to 1.24 V versus RHE at a scan rate of 0.02 V s<sup>-1</sup>. A droplet contact area of  
34  
35 approximately 0.02 cm<sup>2</sup> was assumed for calculation of current density. Chronoamperometry  
36  
37 (CA) measurements at an applied potential of 1.69 V vs RHE for 200 s were used to test OER  
38  
39 stability of films with Mn compositions  $x \geq 0.33$ .  
40  
41  
42  
43

44  
45 Further electrochemical characterization of epoxy-encapsulated Mn<sub>x</sub>Sb<sub>1-x</sub>O<sub>z</sub> electrodes was  
46  
47 conducted after SDC measurements. An electrochemical H-cell was filled with 175 mL of O<sub>2</sub>-  
48  
49 saturated 1.0 M H<sub>2</sub>SO<sub>4</sub> electrolyte (pH 0); a standard calomel reference electrode and carbon rod  
50  
51 counter electrode were separated by a fine-porosity glass frit. A magnetic stir bar and O<sub>2</sub>  
52  
53 bubbling provided constant electrolyte mixing. Measurements were conducted with a Gamry 600  
54  
55  
56  
57  
58  
59  
60

1  
2  
3 potentiostat and Gamry Framework software. The uncompensated resistance of the cell was  
4  
5 determined by electrochemical impedance spectroscopy (EIS) in static 1.0 M H<sub>2</sub>SO<sub>4</sub> electrolyte  
6  
7 at 1.72 V vs RHE in the frequency range of 1 Hz - 300 kHz.  
8  
9

### 10 11 2.3 Theoretical calculations 12

13  
14 To investigate the various possible structures corresponding to the synthesized Mn-Sb oxide  
15  
16 catalysts, density functional theory (DFT) calculations were conducted on a set of intermetallic  
17  
18 oxide phases in the Mn-Sb-O chemical system mined from the Materials Project (MP)  
19  
20 database.<sup>26</sup> In addition, these structures were supplemented with compositional perturbations of  
21  
22 each structure that were generated by combinatorial substitution of 1-2 Mn for Sb and vice versa.  
23  
24 Lastly, two non-Mn containing compounds, rutile TiO<sub>2</sub> and a tri-rutile phase of CoSb<sub>2</sub>O<sub>6</sub> (mp-  
25  
26 24845) were used as templates for an additional set of structures. In the case of TiO<sub>2</sub>  
27  
28 compositional perturbations of a 2×2×2 MnSbO<sub>4</sub> supercell were determined. In the case of  
29  
30 CoSb<sub>2</sub>O<sub>6</sub>, elemental substitutions that spanned every ordered approximation of a disordered  
31  
32 structure of intermetallic oxide phases at compositions of Co<sub>x</sub>Sb<sub>1-x</sub>O<sub>2</sub> were determined for x = 0,  
33  
34 1/6, 1/3, 1/2, 2/3, 5/6, and 1. Relaxation of these structures was performed using automated  
35  
36 VASP DFT routines,<sup>27</sup> resulting in MP-compatible total energies and electron densities. Data  
37  
38 corresponding to the results of these calculations are available on materialsproject.org.  
39  
40 Calculated energies were used to construct compositional phase diagrams in Mn-Sb-O space,  
41  
42 grand potential phase diagrams with a fixed chemical potential of oxygen reflecting stable Mn-  
43  
44 Sb oxides under synthesis conditions, and Pourbaix diagrams to determine the electrochemical  
45  
46 phase stability under OER potentials at acidic pH. Each of these analyses uses pymatgen's phase  
47  
48 and Pourbaix diagram<sup>28</sup> tools directly, and analysis code is available by request. Lastly, Bader  
49  
50 charge calculations<sup>29</sup> were conducted on the calculated charge densities to determine oxidation-  
51  
52  
53  
54  
55  
56  
57  
58  
59  
60



1  
2  
3 state trends between compositions. Additional details about the optimized structures, templates,  
4 and calculation parameters are provided in SI.  
5  
6

## 7 8 9 2.4 Materials Characterization

10  
11 The crystal structures and phase distribution of  $Mn_xSb_{1-x}O_z$  binary composition libraries were  
12 determined by the powder x-ray diffraction (XRD) technique using a Bruker DISCOVER D8  
13 diffractometer with  $Cu K_\alpha$  radiation from a Bruker I $\mu$ S source. The x-ray spot size was limited to  
14 a 1 mm length scale, over which the composition is constant to within approximately 1%. The  
15 XRD measurements were performed on a series of evenly-spaced positions along the  
16 composition gradient. Diffraction images were collected using a two-dimensional VÅNTEC-500  
17 detector and integrated into one-dimensional patterns using DIFFRAC.SUITE™ EVA software.  
18  
19

20  
21 To determine the library composition, x-ray fluorescence (XRF) measurements were performed  
22 on an EDAX Orbis Micro-XRF system with an x-ray beam approximately 2 mm in diameter.  
23 Since the XRF sampling depth far exceeds the film thickness, XRF counts for each element were  
24 assumed to be proportional to the number of corresponding atoms present in the film, and the  
25 sensitivity factor for each element was calibrated using commercial XRF calibration standards  
26 (Micromatter™). These measurements provide evaluation of elemental loss with better than 1%  
27 sensitivity.  
28  
29

30  
31 X-ray photoelectron spectroscopy (XPS) survey spectra were measured to determine the near-  
32 surface chemistry for using a Kratos Axis Ultra with excitation from a monochromatized Al  $K_\alpha$   
33 radiation at 150 W (10 mA at 15 kV). The collected spectra were calibrated to the carbon 1s peak  
34 of 284.8 eV.  
35  
36  
37  
38  
39  
40  
41  
42  
43  
44  
45  
46  
47  
48  
49  
50  
51  
52  
53  
54  
55  
56  
57  
58  
59  
60

1  
2  
3 Ambient pressure XPS (AP-XPS) measurements were performed at Beamline 9.3.2 of the  
4  
5 Advanced Light Source, Lawrence Berkeley National Laboratory.<sup>30</sup> H<sub>2</sub>O adsorption on  
6  
7 samples Mn<sub>0.70</sub>Sb<sub>0.30</sub>O<sub>z</sub> and Mn<sub>2</sub>O<sub>3</sub> were performed by dosing 0.2 Torr H<sub>2</sub>O at 298K, meanwhile  
8  
9 the surface chemistry was investigated by performing the AP-XPS measurements. The low-  
10  
11 resolution survey with a binding energy of 700 eV to -5 eV was collected at an incident photon  
12  
13 energy of 770 eV. The high-resolution Sb 3d and O 1s, and Mn 2p XPS spectra were collected  
14  
15 at an incident photon energy of 670 eV and 770 eV, respectively. For each condition, samples  
16  
17 were equilibrated for at least 90 min before the measurement. By taking spectra at different  
18  
19 sample spots and comparing spectra before and after beam illumination for 2 hours, we found  
20  
21 beam damage on the sample is negligible during the measurements.  
22  
23  
24  
25  
26

27 X-ray absorption spectroscopy (XAS) is an element specific spectroscopic technique and is very  
28  
29 sensitive to oxidation states. The Mn and Sb K-edge XAS measurements were carried out on  
30  
31 beamline 7-3 at the Stanford synchrotron radiation light source (SSRL) along with the standard  
32  
33 references Sb<sup>5+</sup> (Sb<sub>2</sub>O<sub>5</sub>), Mn<sup>2+</sup> (MnO), Mn<sup>3+</sup> (Mn<sub>2</sub>O<sub>3</sub>), Mn<sup>4+</sup> (MnO<sub>2</sub>), and mixed Mn<sup>2+</sup>/Mn<sup>3+</sup>  
34  
35 (Mn<sub>3</sub>O<sub>4</sub>). The quantitative analysis of XAS data was carried out by linear combination fitting  
36  
37 (LCF) using a database of pure-valence species (the Combo method) as reported by Manceau *et*.  
38  
39 *al.*<sup>31</sup> Further details are reported in SI.  
40  
41  
42  
43

44 Inductively coupled plasma mass spectrometry (ICP-MS) was used to determine the  
45  
46 concentration of dissolved metals in electrolyte used for electrochemistry at different durations  
47  
48 over the course of CV cycling. ICP-MS data were collected using an Agilent 7900 ICP-MS. The  
49  
50 composition and loading of the Mn<sub>x</sub>Sb<sub>1-x</sub>O<sub>z</sub> electrode deposited on FTO was obtained by  
51  
52 electrochemically dissolving the film in 27 mL of 20% HNO<sub>3</sub> and cycling the potential with  
53  
54 respect to a carbon rod. The samples were diluted to approximately 2% HNO<sub>3</sub> in milli-Q water.  
55  
56  
57  
58  
59  
60

1  
2  
3 Standard and blanks were prepared in trace metals grade 2% HNO<sub>3</sub> diluted in milli-Q water. The  
4  
5 standard curve included concentrations: 0.1, 1.0, 10.0, 100, 500, and 1000 ppb and were linear  
6  
7 over this range. All sample concentrations fell within the concentration range described by the  
8  
9 calibration curves. The internal standard (Agilent 5188-6525) was used.  
10  
11  
12  
13  
14  
15  
16

### 17 3. RESULTS AND DISCUSSION

#### 18 3.1 Catalyst discovery via combinatorial electrochemistry

19  
20 The OER catalytic activity of Mn<sub>x</sub>Sb<sub>1-x</sub>O<sub>2</sub> composition library was assessed in 1.0 M H<sub>2</sub>SO<sub>4</sub> (pH  
21  
22 0.13) aqueous solution using libraries deposited at 3 different temperatures onto Si substrates  
23  
24 with a Pt conducting layer. Figure S4 shows the series of CVs obtained from the binary  
25  
26 composition library annealed at 700 °C when the applied potential was scanned at 0.02 V s<sup>-1</sup> in  
27  
28 the range of 1.24 to 1.79 V vs RHE. The same CV was performed on a series of compositions  
29  
30 from the library annealed at 550 °C, and 3 cycles of this CV were applied to a series of  
31  
32 compositions from the library that was not annealed after deposition. XRD characterization was  
33  
34 performed on each library and the maximum current from the CVs are plotted with the XRD heat  
35  
36 map in Figure 1.  
37  
38  
39  
40  
41  
42  
43

44 Across the 3 types of processing, the maximum current density not only increases with  
45  
46 decreasing annealing temperature but also becomes more sensitive to film composition due to the  
47  
48 tighter window of rutile alloy formation. The sharp increase in current density at the onset of  
49  
50 rutile crystallization in the as-deposited library is quite striking. Figure 1d also illustrates that for  
51  
52 a given composition, Mn corrosion is lower when the film crystallizes into the rutile structure,  
53  
54 demonstrating that this structure improves both activity and stability, as further discussed below.  
55  
56  
57  
58  
59  
60

1  
2  
3 When the film crystallizes into the rutile structure at the same composition, higher activity is  
4 observed with lower annealing temperature, which may be due to increased nanocrystallinity,  
5 which is a common strategy for creating active catalyst sites.<sup>1b</sup> While these results indicate  
6 opportunities for catalyst optimization via nanostructuring, continued evaluation of the rutile  
7 oxide catalysts in the present work proceeds with annealed films as they are more amenable to  
8 the characterization required to elucidate the underpinnings of the improved activity and  
9 stability.  
10  
11  
12  
13  
14  
15  
16  
17  
18  
19

20 To continue assessment of the initial stability, a subset of samples from the 700 °C library were  
21 measured at 1.69 V vs RHE (460 mV overpotential) for 200 s. The CA data is shown in Figure  
22 S7 and the current at the end of each measurement is shown in Figure 2a, revealing an increase  
23 in current density with increasing Mn concentration for the 4 phase-pure rutile samples, followed  
24 by a slight decrease at  $x = 0.72$  where some  $\text{Mn}_2\text{O}_3$  is present in the as-synthesized film,  
25 confirming that Mn-rich rutile oxide alloys provide the highest catalytic activity.  
26  
27  
28  
29  
30  
31  
32  
33  
34

35 Given the noted variation in catalytic current density with both film composition and phase  
36 behavior, there is no indication that the Pt conducting underlayer contributes meaningfully to the  
37 electrochemical characterization in Figures 1 and 2a, but given the importance of the Sb-Mn  
38 catalyst being free of precious metals, its activity was also validated by depositing a film on an  
39 FTO-coated glass substrate. This conducting layer limits the ability to characterize the catalyst  
40 thin film due to its interference with both XRF and XRD measurements, prompting our target of  
41 approximately  $x = 0.67$  and annealing at 550 °C to provide sufficient XRD intensity to confirm  
42 that the film crystallized in the rutile structure (Figure S1). We performed 40 minutes of  
43 continuous CV cycling of the film, corresponding to 45 cycles as shown in Figure 2b. While  
44 some degradation is observed in the first few cycles, electrocatalytic activity is maintained over  
45  
46  
47  
48  
49  
50  
51  
52  
53  
54  
55  
56  
57  
58  
59  
60

the course of the experiment, with the overpotential required to reach  $10 \text{ mA cm}^{-2}$  increasing by only 15 mV (from 508 to 523 mV) during the measurement.

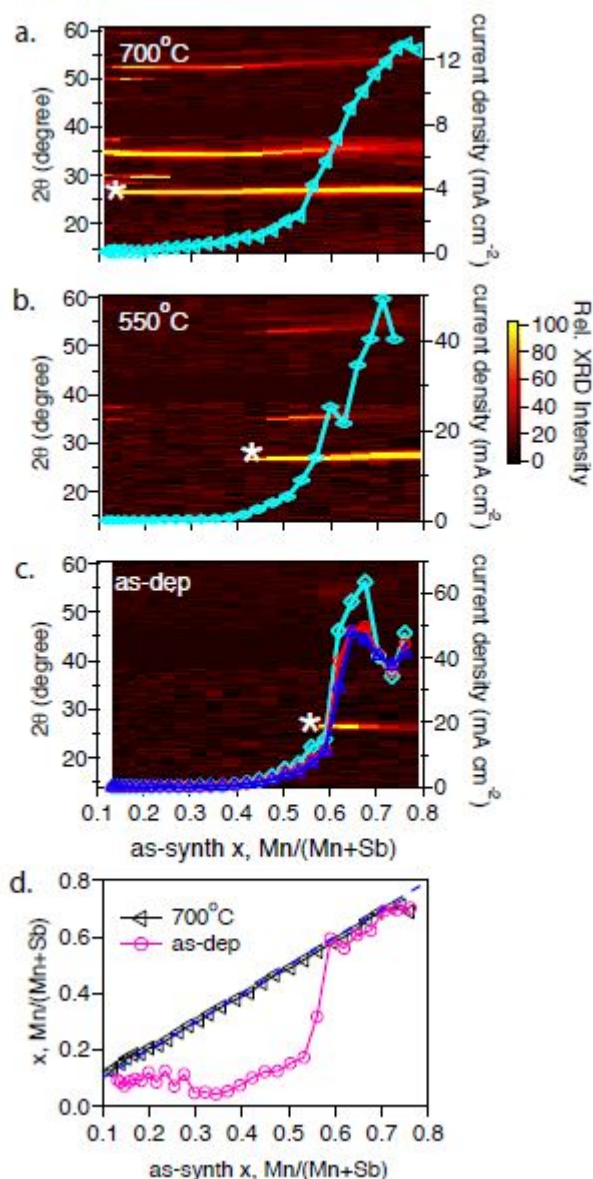


Figure 1. (a-c) 2D XRD plots of 3  $\text{Mn}_x\text{Sb}_{1-x}\text{O}_2$  libraries annealed at  $700^\circ\text{C}$ ,  $550^\circ\text{C}$ , and as-deposited. In each heat map image, each data column corresponds to a 1D XRD pattern at that composition, and the most Sb-rich observation of the rutile [110] peak is indicated with a white \* that moves to higher Mn concentration with decreasing temperature. The current densities obtained at 1.79 V vs RHE in CV measurements on 3 libraries in 1.0 M  $\text{H}_2\text{SO}_4$  aqueous solution

are superimposed on the corresponding XRD maps. For the as-deposited library, 3 consecutive CVs were performed and their maximum current density values are plotted in the order of cyan, red, and blue. (d) XRF-determined composition change after CV measurements for libraries annealed at 700 °C (1 CV cycle) and without annealing (3 CV cycles).

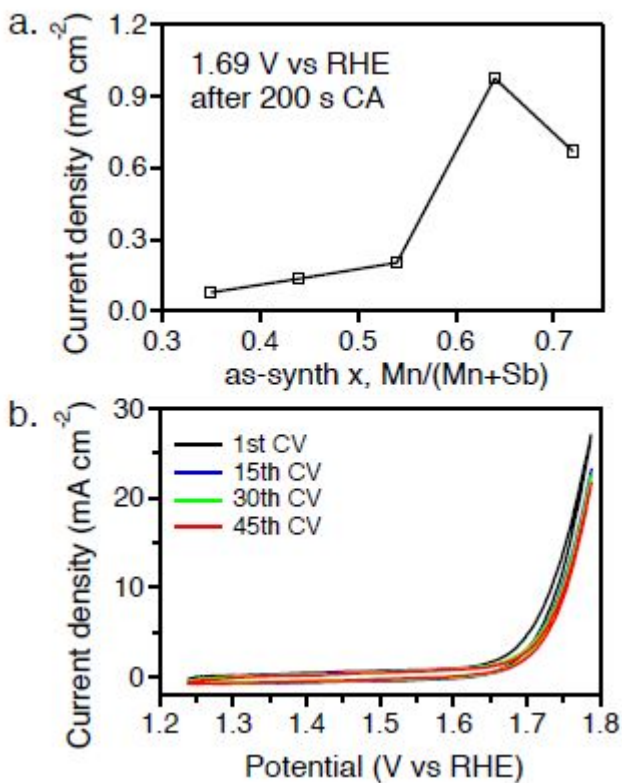


Figure 2. (a) The current density after 200 s CA measurement at 1.69 V vs RHE in 1.0 M H<sub>2</sub>SO<sub>4</sub> aqueous solution (CA data is shown in Figure S7). (b) Current density vs potential for Mn<sub>0.67</sub>Sb<sub>0.33</sub>O<sub>z</sub> film deposited on FTO and annealed at 550 °C in 1.0 M H<sub>2</sub>SO<sub>4</sub> solution initially (1<sup>st</sup> CV) and after 15, 30, and 45 CV sweeps between 1.24 and 1.79 V vs RHE at a scan rate of 0.02 V s<sup>-1</sup>.

### 3.2 Stability of catalyst activity and composition

Further evaluation of operational stability was performed by operating larger samples in a traditional electrochemical H-cell with carbon counter electrode. A 1.75 cm<sup>2</sup> electrode

1  
2  
3 containing FTO-supported  $\text{Mn}_{0.70}\text{Sb}_{0.30}\text{O}_z$  (composition determined by ICP-MS) annealed at  
4  
5 550 °C was cycled between 1.23 and 1.83 V vs RHE (uncompensated) at 0.02 V s<sup>-1</sup>. Over the  
6  
7 course of 4320 CV cycles, aliquots of electrolyte were extracted to quantify the dissolved  
8  
9 concentrations of Sb and Mn via ICP-MS. The electrolyte was replaced after 6 hours of testing to  
10  
11 confirm that catalytic activity continued after returning the metals concentrations to near zero.  
12  
13 Similar experiments were performed on a  $\text{Mn}_2\text{O}_3$  electrode for comparison, with measurements  
14  
15 stopped after 40 cycles due to loss of activity. The results are summarized in Figure 3, revealing  
16  
17 that the initial high current density provided by  $\text{Mn}_2\text{O}_3$  quickly decays due to corrosion of 87%  
18  
19 of the deposited Mn within 40 CV cycles. The  $\text{Mn}_{0.70}\text{Sb}_{0.30}\text{O}_z$  degrades much more slowly with  
20  
21 loss of approximately half of the 170 nm film after 4000 cycles, which corresponds to loss of  
22  
23 approximately 0.1 monolayer per cycle, which exposes a new catalyst surface that is likely  
24  
25 similar to the as-synthesized catalyst. The ICP-MS measurements also included complete  
26  
27 digestion of the Sb-Mn catalyst film after testing as well as testing of the counter electrode and  
28  
29 electrolyte to confirm the absence of precious metals up to the detectability limit of ~1 ppb.  
30  
31  
32  
33  
34  
35

36 Stability measurements with less CV cycling were performed on a 0.22 cm<sup>2</sup> electrode containing  
37  
38 Pt-supported  $\text{Mn}_{0.67}\text{Sb}_{0.33}\text{O}_z$  (composition determined by XRF) annealed at 700 °C. In addition,  
39  
40 an epoxy-encapsulated electrode of the Pt/Ti/SiO<sub>2</sub>/Si substrate (0.34 cm<sup>2</sup>) was fabricated as a  
41  
42 control sample to confirm that the conductive Pt underlayer does not contribute to the  
43  
44 electrochemical characterization of the Sb-Mn catalyst (see Figure S18). The series of CV, CA,  
45  
46 chronopotentiometry (CP), and open circuit potentiometry (OCP) measurements performed on  
47  
48 the Mn-Sb catalyst is summarized in Figure 4, including approximately 27 hours of CA  
49  
50 experiments at 1.72 V vs RHE along with two CV cycles acquired after both 2 hours and 25  
51  
52 hours of CA measurements. The Sn-free electrode enabled quantification of elemental corrosion  
53  
54  
55  
56  
57  
58  
59  
60

1  
2  
3 from XRF characterization of the film before and after electrochemical operation, as summarized  
4  
5 in Figure S20 and Table S3, revealing substantially less corrosion than that observed in Figure  
6  
7 3c, with 3.8% of Sb and 25% of Mn corroded after approximately 30 hours of electrochemical  
8  
9 operation. This disparity in elemental corrosion from the 409 nm film indicates that the  
10  
11 equivalent of ~5 nm of Sb oxide dissolves while Mn dissolves from at least 100 nm of as-  
12  
13 synthesized film thickness, indicating that slow Mn corrosion proceeds via diffusion through a  
14  
15 Sb-rich surface. The resistance-compensated CVs in Figure 4b reveal the excellent  
16  
17 electrocatalytic activity with current density exceeding  $50 \text{ mA cm}^{-2}$  at 0.58 V overpotential. The  
18  
19 low-current-density portion of the log-scale CV indicates that the onset of catalytic current is  
20  
21 near 0.3 V overpotential, while the high-current-density portion ( $0.1\text{-}100 \text{ mA cm}^{-2}$ ) shows a  
22  
23 Tafel slope of about  $75 \text{ mV dec}^{-1}$ .  
24  
25  
26  
27  
28

29 Figure 4a shows consistent current density above  $0.5 \text{ mA cm}^{-2}$  intermixed with a series of current  
30  
31 transients which occur whenever the potentiostat is turned off to create an open circuit condition.  
32  
33 When the open circuit duration is on the order of 1 minute, the initial current density upon  
34  
35 reapplication of the CA voltage is approximately  $1 \text{ mA cm}^{-2}$ ; longer open circuit durations (40  
36  
37 minutes) restore the current density to approximately the initial value of  $3 \text{ mA cm}^{-2}$ . To further  
38  
39 probe this phenomena, Figure 4c contains additional experiments starting with a 20 min OCP  
40  
41 measurement which reveals that upon introduction to the electrolyte the open circuit potential is  
42  
43 near the OER Nernstian potential. After a 2 hour CA at 1.72 V vs RHE, the subsequent 20 min  
44  
45 OCP starts at a higher value that decreases on the scale of 10 minutes; this change in OCP  
46  
47 indicates a change to the catalyst surface that is responsible for the initial transients in activity for  
48  
49 each CA measurement in Figures 4a and 4c. While this ability to recover activity at open circuit  
50  
51 seems desirable, the deployment of this catalyst to attain stable OER operation hinges upon  
52  
53  
54  
55  
56  
57  
58  
59  
60



1  
2  
3 understanding the mechanism of current density restoration, particularly given the observation  
4 from Figure 3b that voltage cycling accelerates Sb and Mn dissolution.  
5  
6

7  
8 To better quantify the differences in stability both between  $\text{Mn}_2\text{O}_3$  and the Mn-Sb oxide alloy  
9 and between CV cycling and operation at more static potential, the total charge passed during  
10 respective measurements were compared with the amount of corroded Mn and Sb to determine  
11 the number of OER turnovers ( $4 e^-$  per  $\text{O}_2$ ) per corroded Mn (assumed  $2 e^-$  per Mn, see SI) and  
12 per corroded Sb (assumed  $1 e^-$  per Sb, see SI). This quantity is similar to the turnover number  
13 (not turnover frequency) indicating the number of catalytic cycles before deactivation. The  
14 results in Table 1 demonstrate that the Mn-Sb catalyst provides a 40-fold improvement over  
15  $\text{Mn}_2\text{O}_3$  in the generated  $\text{O}_2$  per corroded Mn ion during CV cycling. The catalyst operated  
16 primarily under CA and CP modes exhibits an additional  $\sim 100$ -fold improvement, although  
17 notably this sample also differs in its substrate and annealing temperature. The low Sb corrosion  
18 during this measurement results in  $10^4$   $\text{O}_2$  per corroded Sb. The stoichiometric phase  $\text{MnSb}_2\text{O}_6$ ,  
19 corresponding to the  $x = 0.33$  sample in this work, was recently reported as an OER catalyst in  
20  $1.0 \text{ M H}_2\text{SO}_4$  electrolyte and 60% Mn loss was observed over 168 hours of CP operation,<sup>16d</sup>  
21 indicating that substantial Mn loss also occurs in Sb-rich compositions and motivating more  
22 detailed assessment of the thermodynamics of Mn-Sb rutile oxides.  
23  
24  
25  
26  
27  
28  
29  
30  
31  
32  
33  
34  
35  
36  
37  
38  
39  
40  
41  
42  
43  
44  
45  
46  
47  
48  
49  
50  
51  
52  
53  
54  
55  
56  
57  
58  
59  
60

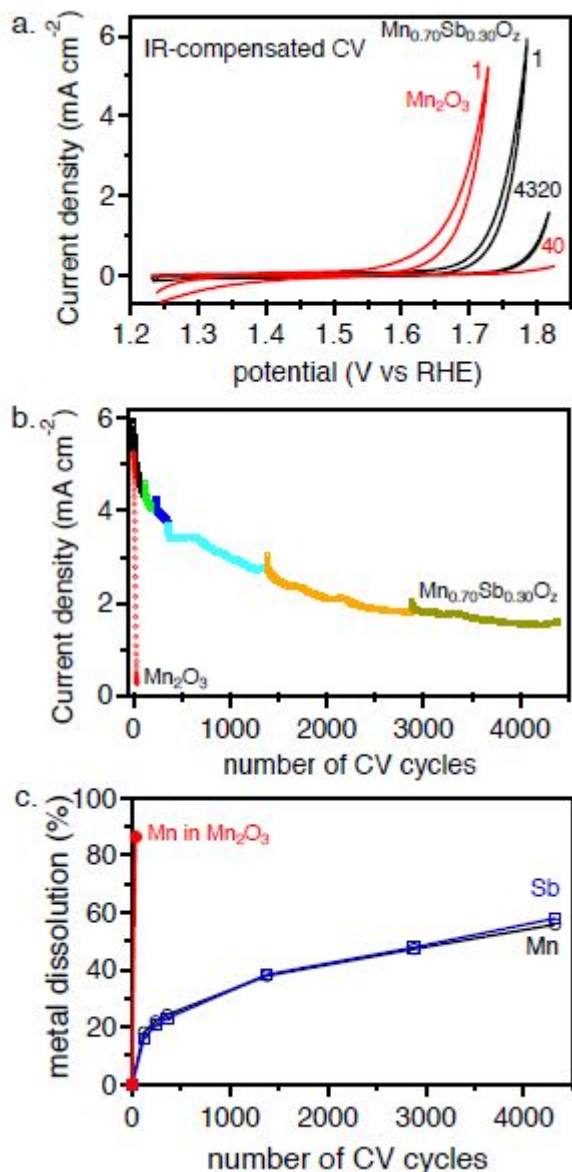


Figure 3. (a) IR-compensated CVs in 1.0 M H<sub>2</sub>SO<sub>4</sub> solution between 1.23 and 1.83 V vs RHE at a rate of 0.02 V s<sup>-1</sup> of two epoxy-encapsulated electrodes: Mn<sub>0.70</sub>Sb<sub>0.30</sub>O<sub>2</sub> and Mn<sub>2</sub>O<sub>3</sub>, which were both deposited on FTO and annealed at 550 °C (see Figure S16 for non-IR-compensated CVs). (b) The current density obtained at the maximum potential in each CV cycle for both Mn<sub>0.70</sub>Sb<sub>0.30</sub>O<sub>2</sub> and Mn<sub>2</sub>O<sub>3</sub> electrodes. (c) The cumulative fraction of dissolved metals as determined by ICP-MS measurements of the electrolyte.

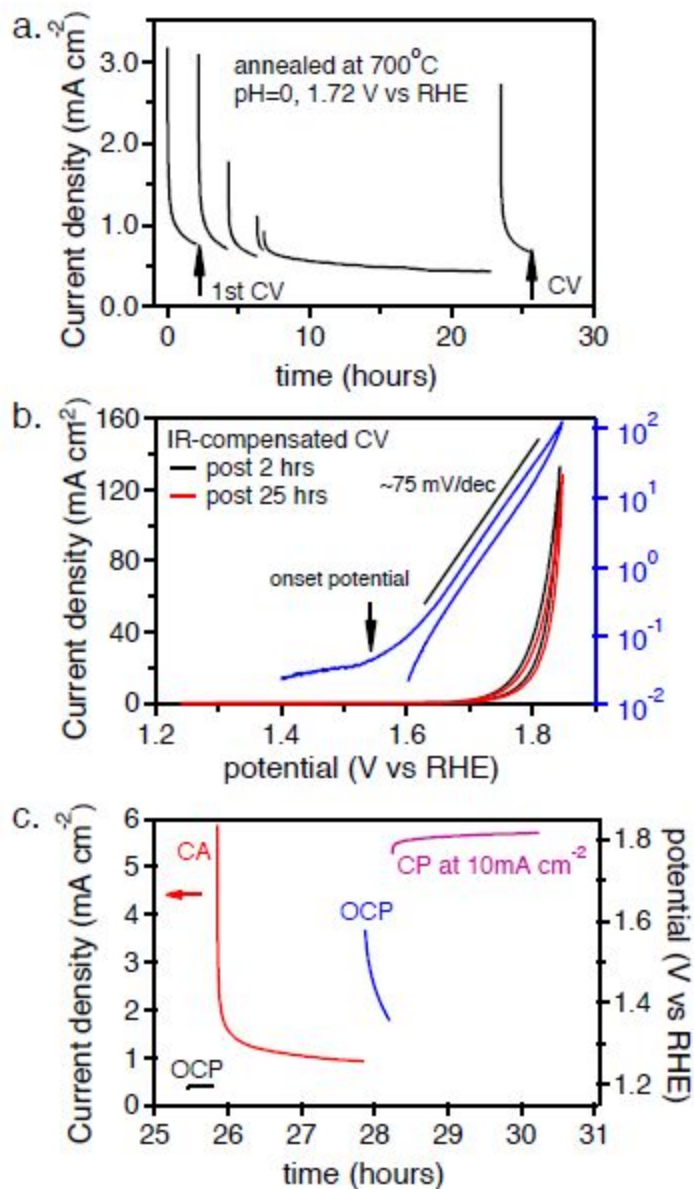


Figure 4. (a) A series of CA measurements at 1.72 V vs RHE (490 mV overpotential) in 1.0 M  $\text{H}_2\text{SO}_4$  solution of epoxy-encapsulated rutile  $\text{Mn}_{0.67}\text{Sb}_{0.33}\text{O}_z$  electrode annealed at 700 °C. (b) Two IR-compensated CVs at  $0.01 \text{ V s}^{-1}$  in between CA measurements, one is after 2 hours and the other is at the end of about 25 hours of catalyst operation, which is also plotted in log-scale in blue color (see Figure S19 for non-IR-corrected CVs). (c) A subsequent batch of experiments on the same electrode where another 2 hour CA measurement between two 20 min open circuit potential (OCP) measurements shows the decrease in current density during the CA is concurrent with an increase in the open circuit potential, which then “recovers” on the time scale of 10 minutes at open circuit. These measurements are followed by a 2 hour chronopotentiometry (CP)

measurement at current density of  $10 \text{ mA cm}^{-2}$  that is fairly stable at an overpotential of 586 mV for the final hour.

Table 1: Analysis of the total anodic charge from stability testing of a Mn oxide and 3 Sb-Mn oxide electrodes. Using XRF and/or ICP-MS to determine the dissolved Mn and Sb concentrations, and assuming  $2 e^-$  per Mn and  $1 e^-$  per Sb corrosion processes, the total OER charge was used to quantify the amount of  $\text{O}_2$  produced, which was then divided by the respective number of corroded metal atoms.

As-synth comp.	Fig.	Conducting layer	Anneal temp. ( $^{\circ}\text{C}$ )	CA+CP time (hours)	CV cycles	Total charge (C)	$\text{O}_2$ per corroded Mn	$\text{O}_2$ per corroded Sb
$\text{Mn}_1$	3	FTO	550		40	0.872	2.0	
$\text{Mn}_{0.67}\text{Sb}_{0.33}$ *	2	FTO	550		45	0.078	71	
$\text{Mn}_{0.70}\text{Sb}_{0.30}$	3	FTO	550		3240	19.444	86	$1.9 \cdot 10^2$
$\text{Mn}_{0.67}\text{Sb}_{0.33}$	4	Pt	700	29	2	31.626	$7.5 \cdot 10^2$	$1.0 \cdot 10^4$

\* This composition was not measured due to overlap of the XRF Sb peak with Sn peak from the FTO layer. The composition was estimated based on XRD data and comparisons to other libraries.

### 3.3 Computational assessment of solid state and aqueous stability

Computational assessment of Mn-Sb rutile oxides commenced with solid state stability as a function of alloy composition, particularly because the rutile phase has only been previously observed at Mn concentrations up to  $\text{Mn}_{0.5}\text{Sb}_{0.5}\text{O}_2$ ,<sup>32</sup> so our observation of continued alloying up to  $x = 0.70$  constitutes the discovery of new phase behavior in this composition space. To evaluate the phase stability of rutile alloys, supercells containing 6 cation sites were populated with Sb and/or Mn to create a series of 7 compositions:  $x = 0, 1/6, 1/3, 1/2, 2/3, 5/6, 1$ . A  $2 \times 2 \times 2$  supercell of rutile  $\text{TiO}_2$  (substituted at  $x = 1/2$  to form  $\text{MnSbO}_4$ ) is also considered as a template, with compositional perturbations yielding structures with formula  $\text{Mn}_x\text{Sb}_{1-x}\text{O}_2$  where  $x = 3/8, 7/16, 1/2, 9/16, 5/8$ . The formation energy ( $\Delta E_{form}$ ) for each phase is shown in Figure 5 along with the non-rutile phases from the Materials Project database, revealing that a rutile alloy lies on

1  
2  
3 the convex hull only at  $x = 1/2$ . At  $x = 1/3$ , the hexagonal phase  $\text{MnSb}_2\text{O}_6$  is energetically more  
4 favorable with formation energy only 20 meV/formula unit below the rutile structure, which is  
5 well within the characteristic 80 meV/formula unit window of the GGA-based above-hull energy  
6 where most synthesizable phases are found.<sup>33</sup> Rutile alloys exist in this 80 meV/formula unit  
7 above-hull window from approximately  $x = 1/3$ , which matches our experimental observation of  
8 the rutile alloy phase boundary with 700 °C annealing, to approximately  $x = 2/3$ , which is in  
9 good agreement with our experimental value of  $x = 0.70$ .

10  
11 This series of rutile oxide alloys also enables evaluation of the thermodynamic enhancement in  
12 Mn stability provided by the Sb-Mn rutile oxide (Figure 3 and Table 1). Stability analysis for  
13 OER conditions in strong acid was assessed with Pourbaix calculations using the recently-  
14 developed formalism for calculating the above-hull energy for a given material as a function of  
15 pH and potential.<sup>28b</sup> Figure 6a shows the calculated Pourbaix above-hull energies at pH 0 for 3  
16 Mn-Sb rutile alloys (with composition of  $x = 1/3$ ,  $1/2$ , and  $2/3$ ), revealing that all three Mn-Sb  
17 compositions ( $\text{MnSb}_2\text{O}_6$ ,  $\text{MnSbO}_4$ , and  $\text{Mn}_2\text{SbO}_6$ ) are thermodynamically more stable than  $\text{IrO}_2$   
18 in strong acid at moderate overpotential, although these results do not account for any  
19 differences in corrosion kinetics. Since the Mn-Sb catalysts need to be operated at higher  
20 overpotentials, the energy above hull at OER operation is similar for  $\text{IrO}_2$  and these precious-  
21 metal-free catalysts.

22  
23 Figures 6b and 6c contain the resulting Pourbaix above-hull energy for the tri-rutile phase  
24  $\text{MnSb}_2\text{O}_6$  ( $x = 1/3$ ) and the rutile alloy  $\text{Mn}_2\text{SbO}_6$  ( $x = 2/3$ ) with Mn and Sb ion concentrations  
25 each fixed at  $10^{-9}$  M. The corresponding Pourbaix diagrams show that the  $x = 1/2$  rutile alloy  
26  $\text{MnSbO}_4$  is thermodynamically stable in strong acid for moderate OER overpotentials. Since the

1  
2  
3 Mn-rich alloys from the solid state stability analysis of Figure 5 do not lie on the convex hull of  
4  $\Delta E_{form}$ , they cannot appear in the Pourbaix hull and thus cannot appear in the Pourbaix diagram.  
5  
6 Figure 6c shows that at 1.5 V vs RHE, just below the OER onset potential noted above,  
7  
8  $Mn_2SbO_6$  has a small driving force for decomposing into  $MnSbO_4$  and  $MnO_2$  solids, which arises  
9  
10 only from the difference in  $\Delta E_{form}$  shown in Figure 5 and indicates that no corrosion will occur  
11  
12 under these electrochemical conditions. At higher and lower OER potentials, the Pourbaix  
13  
14 analysis predicts that Mn will corrode as  $MnO_4^-$  and  $Mn^{+2}$ , respectively, indicating that  
15  
16 substantially improved stability may be obtained through catalyst optimization to slightly lower  
17  
18 the onset potential and enable stable operation under tight potential control.  
19  
20  
21  
22  
23  
24

25 The Pourbaix analysis of Figure 6 also indicates that under the potential range of the CVs in  
26  
27 Figures 2-4, Sb is thermodynamically stable, in contradiction to the observed Sb dissolution  
28  
29 under CV cycling. The corrosion curves of Figure 3c demonstrate that Sb and Mn are dissolved  
30  
31 in proportion to the film composition. With no candidate electrochemical pathways for this  
32  
33 dissolution, this degradation may be mechanical in nature, which we explore by calculating the  
34  
35 Sb-atom normalized ratios between the volumes of  $Sb_2O_5$  and  $Mn_xSb_{1-x}O_6$ . These values,  
36  
37 analogous to the Pilling-Bedworth ratios, are 0.89, 0.76, and 0.57 for  $x = 1/3, 1/2,$  and  $2/3,$   
38  
39 respectively, and suggest that corroding Mn from the near-surface will create increasing  
40  
41 compressive strain with increasing Mn in the as-synthesized film material, which makes the Mn-  
42  
43 rich compositions more susceptible to any mechanical degradation that is triggered by CV  
44  
45 cycling. This possibility of mechanical degradation not only highlights the importance of  
46  
47 optimizing catalyst morphology in future development, but also underscores the difference in  
48  
49 degradation during CV cycling compared to the diffusion-limited Mn corrosion that occurs  
50  
51 during catalyst operation at appreciable overpotential.  
52  
53  
54  
55  
56  
57  
58  
59  
60

Another key observation from Figure 6a is that under OER potentials, the Sb-Mn rutile oxides are more stable than  $\text{Mn}_2\text{O}_3$  by 0.5 to 1 eV/atom. Considering that  $\text{Sb}_2\text{O}_5$  is stable under these conditions, this thermodynamic stabilization can be viewed as a stabilization of the Mn, motivating investigation of the presence of low valent Mn in the Mn-Sb rutile oxide catalyst, which is pursued below.

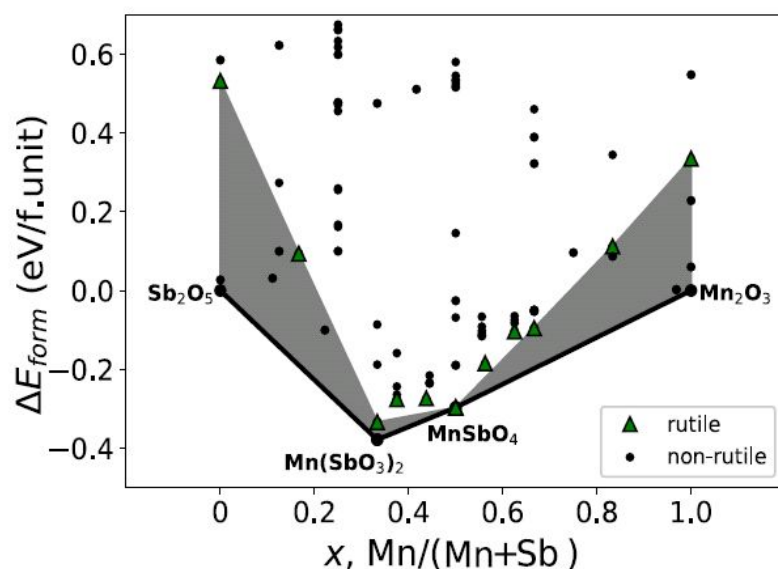


Figure 5. Grand potential phase diagram: calculated formation energy ( $\Delta E_{form}$ ) variation with the composition for phases in Mn-Sb-O system at 700 °C and 0.2 atm  $\text{O}_2$ , in addition to the rutile structure  $\text{TiO}_2$  and tri-rutile  $\text{CoSb}_2\text{O}_6$ . The rutile and non-rutile phases are indicated with green triangles and black circles, respectively. The non-rutile phases in Mn-Sb-O system are provided in Figure S21, SI. The shaded region indicates the above hull energy of the rutile structures.

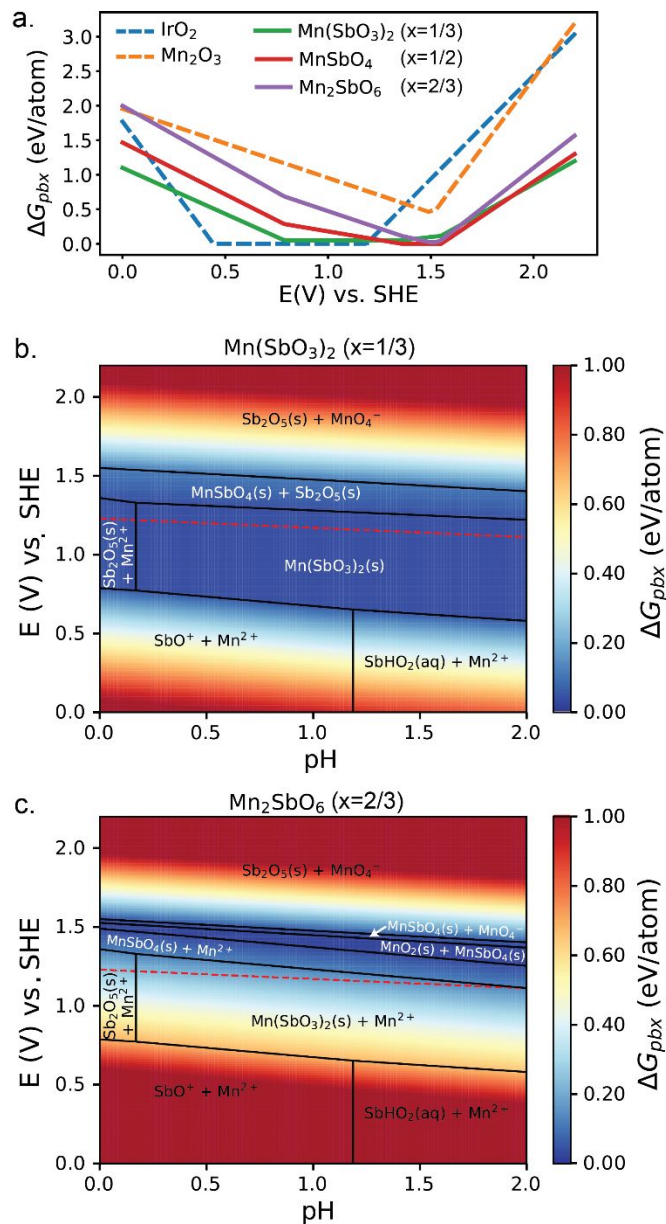


Figure 6. (a) Calculated Gibbs free energy above hull at pH 0 for 3 Mn-Sb rutile alloys at  $x = 1/3, 1/2,$  and  $2/3$ , respectively, along with  $\text{Mn}_2\text{O}_3$  and  $\text{IrO}_2$  as comparison in the potential range of 0 – 2.2 V vs SHE. The moderate overpotential portion of Pourbaix above-hull energy reveals that all 3 Mn-Sb rutile alloys are more thermodynamically stable than  $\text{IrO}_2$  in strong acid. Computationally predicted Pourbaix diagram of Sb-Mn-O system at pH = 0 - 2 range for Mn content (b)  $x = 1/3$  and (c)  $x = 2/3$ , respectively. The Mn and Sb ion concentrations each fixed at  $10^{-9}$  M. The Gibbs free energy ( $\Delta G_{pbx}$ ) of the rutile  $\text{MnSb}_2\text{O}_6$  and  $\text{Mn}_2\text{SbO}_6$  with respect to the



Pourbaix stable phases is superimposed on the corresponding Pourbaix diagram and represented by the color bar. The red dashed lines denote potential of 1.23 V vs RHE (OER potential).

### 3.4 Identification of low valent Mn and its mechanistic importance

Characterization of the ionic composition of the Mn-Sb rutile oxides commenced with XAS characterization of 4 samples after the 200 s CA measurements in Figure 2a (post-electrochemistry samples), as well as 4 as-synthesized samples with  $x = 0.35, 0.38, 0.53,$  and  $0.69$ . As seen in Figure 7a, there is no measurable change of Sb K-edge signal over the range of composition measured, and the Sb XAS signal is unaffected by the 200 s CA measurement, corroborating the electrochemical stability of Sb. All of the Sb K-edge spectra match well with the reference of  $\text{Sb}_2\text{O}_5$  indicating that Sb is present as  $\text{Sb}^{+5}$  across the entire composition range of rutile alloy  $\text{Mn}_x\text{Sb}_{1-x}\text{O}_2$ . More variability is observed in the Mn XAS signals (Figure 7b), and importantly the variability is primarily a function of as-synthesized composition and not introduced by the 200 s CA measurement. This indicates that while some Mn corrodes from the film, the remaining Mn does not experience any irreversible electrochemical oxidation during catalyst operation. Each Mn K-edge spectrum exhibits an absorption edge energy that increases with Mn concentration in the rutile alloy but remains between that of the  $\text{Mn}^{+2}$  and  $\text{Mn}^{+3}$  reference spectra, corresponding to an increase in the average Mn oxidation state with increasing  $x$ , as shown in Figure 8.

If the rutile alloy maintains a 2 oxygen per cation stoichiometry, and the O and Sb remain in their respective -2 and +5 formal oxidation states, charge balance requires the average oxidation state of Mn in  $\text{Mn}_x\text{Sb}_{1-x}\text{O}_2$  alloy to be  $5-x^{-1}$ , as shown in Figure 8. At  $x = 1/3$ , this gives the  $\text{Mn}^{+2}$  reported<sup>32a</sup> to exist in the tri-rutile  $\text{MnSb}_2\text{O}_6$  and predicts that the average Mn oxidation state

1  
2  
3 would exceed +3 within our observed rutile alloy composition window. While the XAS results  
4 share the qualitative behavior of increasing Mn oxidation with increasing Mn concentration,  
5 which is further corroborated by Bader charge analysis of the computational structures (Figure  
6 S14), the +3 value is only reached at the phase boundary of the Mn-saturated rutile alloy and  
7  
8  
9  
10  
11  
12  $\text{Mn}_2\text{O}_3$ .

13  
14  
15 The low average Mn oxidation state at high Mn concentrations suggests that the Mn-rich rutile  
16 alloys exhibit some combination of O vacancies and/or covalent Mn-O bonding that corresponds  
17 to deviations from the formal integer valences. The formation energy for an O vacancy was  
18 evaluated with supercell calculations (Figure S22) revealing above-hull energies as low as 0.16  
19 eV/formula unit near  $x = 0.5$  with higher above hull energies at both Mn-rich and Sb-rich rutile  
20 oxide compositions, which does not plausibly explain the observations of Figure 8 considering  
21 that balancing charge for the Mn-rich compositions would require about 10% of  $\text{O}^{2-}$  sites to be  
22 vacant. Analysis of the relative Bader charge for O in the rutile oxide supercells (Figure S14)  
23 reveals that its absolute value decreases and becomes more variable over the 12 supercell sites as  
24 the Mn concentration increases, which is an indicator of increasing Mn-O covalency in the Mn-  
25 rich rutile oxide alloys. Formation of  $\text{Mn}^{+4}$  would enabled more ionic bonding, and some  
26 intuition for the absence of this phenomenon can be gained from analysis of ionic radii  
27 considering that  $\text{Mn}^{+4}$  has about 10% lower ionic radius than the approximately equal radii of  
28  $\text{Sb}^{+5}$  and  $\text{Mn}^{+3}$ .<sup>34</sup> To further characterize the Mn-O bonds, we return to the XAS characterization  
29 where the Mn-K extended x-ray absorption fine structure (EXAFS) signals were generated for  
30 the most Sb-rich and Mn-rich as-synthesized samples from Figure 7 and analyzed by fitting the  
31 first coordination shell (Figure S12). For  $x = 0.35$ , the fitted Mn-O bond distance for  $\text{MnO}_6$   
32 octahedra was 2.13 Å, whereas two Mn-O bond distances (approximately 1.9 Å and 2.2 Å) were  
33  
34  
35  
36  
37  
38  
39  
40  
41  
42  
43  
44  
45  
46  
47  
48  
49  
50  
51  
52  
53  
54  
55  
56  
57  
58  
59  
60

1  
2  
3 required to fit the EXAFS data at  $x = 0.72$ . This variation in the Mn-O bond distance is in good  
4  
5 agreement with the supercell rutile model at  $x = 0.67$ , which has ~3% larger volume due to 3%  
6  
7 larger value of the  $c$  lattice parameter compared to experiment (see Figure S13). In this 18 atom  
8  
9 supercell, the Mn-O distances range from 1.93 to 2.04 Å, and the Mn-Mn nearest neighbor  
10  
11 distances vary from 2.97 to 3.56 Å. Collectively, these results are consistent with Jahn-Teller  
12  
13 distortions that are common to  $\text{Mn}^{+3}$  oxides and indicate that the catalyst contains a mixture of  
14  
15 edge-sharing and corner-sharing  $\text{Mn}^{+3}\text{O}_6$  octahedra.<sup>20, 36</sup>  
16  
17  
18  
19

20 While the Pourbaix analysis combined with XAS analysis highlights the stabilization of  $\text{Mn}^{+3}$   
21  
22 under OER conditions in the Sb-Mn catalyst, direct observation of surface species during catalyst  
23  
24 operation is notoriously difficult. We performed the related measurement of XPS analysis of the  
25  
26 near surface chemistry after OER operation, both in vacuum and under exposure to  $\text{H}_2\text{O}$ , the  
27  
28 latter measurement enabled by recent development of ambient pressure XPS (AP-XPS).<sup>30</sup> An  
29  
30 electrode similar to that of Figure 3 was cycled 50 times between 1.23 and 1.83 V vs RHE (same  
31  
32 as Figure 3) and subsequently cut from the epoxy-sealed electrode for XPS analysis. The survey  
33  
34 scan in Figure 9a shows approximately equal concentrations of Sb and Mn in the near-surface  
35  
36 region. The measurement was also performed on an as-synthesized  $\text{Mn}_2\text{O}_3$  film to enable  
37  
38 comparison of the Mn oxidation state. The inset shows the Mn 3s doublet from each material,  
39  
40 and the 5.4 eV peak splitting for the  $\text{Mn}_2\text{O}_3$  film is just below the literature value of 5.5 eV<sup>35</sup> for  
41  
42  $\text{Mn}^{+3}$ , indicating an average oxidation state above +3. The higher 5.6 eV splitting from the post-  
43  
44 electrochemistry Mn-Sb catalyst indicates an average oxidation state below +3 (literature value  
45  
46 for  $\text{Mn}^{+2}$  peak splitting is 5.9 eV), demonstrating that the mixture of  $\text{Mn}^{+2}$  and  $\text{Mn}^{+3}$  in the bulk  
47  
48 (Figures 7-8) also appears in the near-surface region, likely with a higher prevalence of  $\text{Mn}^{+3}$ . To  
49  
50 assess whether this mixture of  $\text{Mn}^{+2}$  and  $\text{Mn}^{+3}$  oxidizes upon water exposure, AP-XPS of the Mn  
51  
52  
53  
54  
55  
56  
57  
58  
59  
60

1  
2  
3 2p region was performed in 0.2 Torr H<sub>2</sub>O where the signal appeared stable over 90 minutes of  
4 water exposure. Figure 9b compares this signal to that measured in vacuum before water  
5 exposure. While the Mn 2p peak positions for Mn<sup>+2</sup> and Mn<sup>+3</sup> are similar, the distinguishing  
6 feature of Mn<sup>+2</sup> is a satellite feature that is observed in the vacuum measurement and still  
7 observed with somewhat lower intensity upon water exposure. There is no indication of  
8 oxidation to Mn<sup>+4</sup>, with these results corroborating the Pourbaix and XAS analysis that Mn<sup>+2</sup> and  
9 Mn<sup>+3</sup> exist in the near-surface region and are resistant to oxidation.  
10  
11  
12  
13  
14  
15  
16  
17  
18  
19

20 The OER environment is more oxidizing than the AP-XPS environment, making the Pourbaix  
21 analysis the most definitive characterization of stable Mn species, from which the 0.5-1 eV/atom  
22 stabilization of Mn<sup>+3</sup> is the most distinguishing feature of the Mn-Sb rutile oxides, which is in  
23 excellent agreement with present understanding of the importance of Mn<sup>+3</sup> in catalyzing the  
24 OER.<sup>20b, 21, 36</sup> Mn<sup>3+</sup> octahedra, both in corner-sharing and edge-sharing configurations, have  
25 been established as the predominant active species through extensive analysis of Mn oxide and  
26 hydroxide OER catalysts.<sup>20, 36</sup> As noted above, the Mn-rich rutile oxides have both corner and  
27 edge sharing octahedral, which explains why stabilization of Mn<sup>+3</sup> is critical for realizing its  
28 OER activity in strong acid. The increasing Mn-O covalency in the Mn-rich rutile oxide alloys,  
29 which exhibit the highest activity, is in excellent agreement with previous analysis of  
30 electrochemically activated Mn<sup>3+</sup> in acid, for which the OER activity is attributed to a reduction  
31 in the HOMO-LUMO gap that increases the metal-oxygen covalency and therefore increases the  
32 equilibrium concentration of reactive oxyl radical species.<sup>21, 37</sup> Through analysis of variation in  
33 OER reaction mechanism with electronic structure of transition-metal oxides (including multi-  
34 metal oxides), the metal-oxygen covalency was determined to be a key differentiator between the  
35 conventional coupled electron-proton transfer mechanism and a mechanism in which non-  
36  
37  
38  
39  
40  
41  
42  
43  
44  
45  
46  
47  
48  
49  
50  
51  
52  
53  
54  
55  
56  
57  
58  
59  
60

1  
2  
3 concerted proton-electron transfer is coupled to lattice oxygen activation.<sup>38</sup> The increased Mn-O  
4 covalency of the Mn-rich rutile oxides, as identified by Bader charge and XAS analyses,  
5  
6 indicates that OER proceeds via the non-concerted mechanism on the Mn-Sb rutile oxides, which  
7  
8 explains the sharp increase in activity with increasing Mn concentration and crystallization into  
9  
10 the rutile structure (Figure 1).  
11  
12  
13  
14  
15

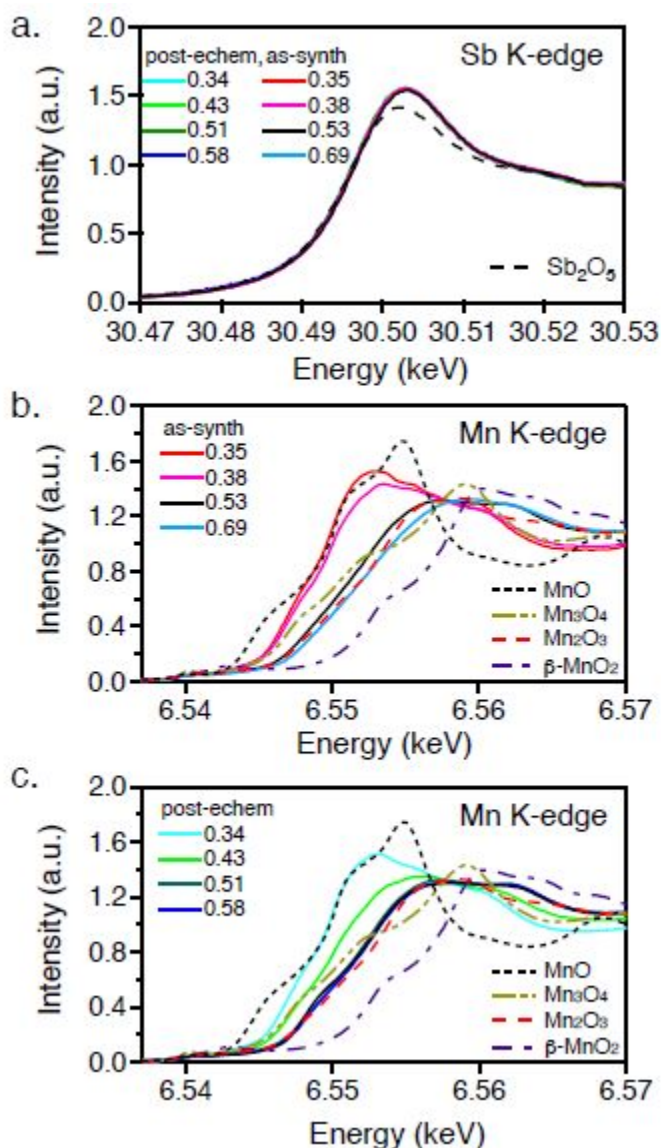


Figure 7. (a) Sb and (b-c) Mn K-edge XAS spectra of rutile alloy  $\text{Mn}_x\text{Sb}_{1-x}\text{O}_2$  at a series of Mn concentrations for both as-synthesized and post-electrochemistry films. The reference antimony and manganese oxides with known oxidation states are shown in dashed lines.

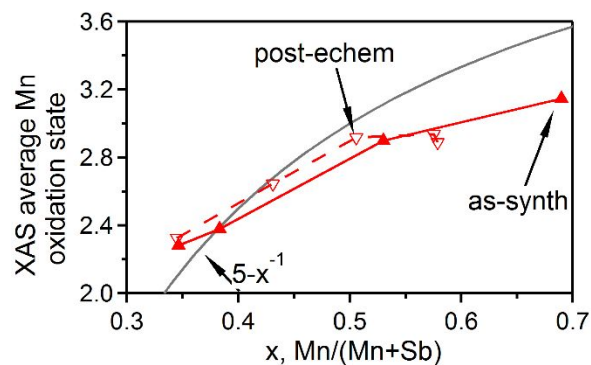


Figure 8. The average Mn oxidation state derived from XAS measurements for both as-synthesized and post-electrochemistry films, showing a marked increase in Mn oxidation state with increasing Mn concentration. The formal Mn oxidation state corresponding to  $y$  in  $\text{Mn}^y_x\text{Sb}^{+5}_{1-x}\text{O}_{-2}$  is also shown in gray. Note that the post-electrochemistry samples are plotted according to their post-electrochemistry XRF values of  $x$ .

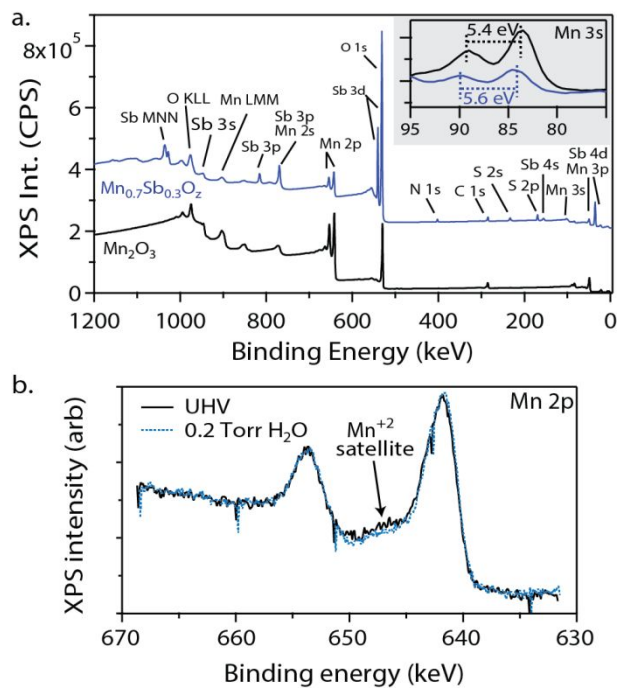


Figure 9. XPS analysis of a  $\text{Mn}_2\text{O}_3$  film (as-synthesized) and  $\text{Mn}_{0.70}\text{Sb}_{0.30}\text{O}_z$  sample after 50 CVs in 1 M  $\text{H}_2\text{SO}_4$  (see Figure S15). (a) Survey scan shows the as-synthesized elements as well as S from the electrolyte. Analysis of the Mn 2p and Sb  $3d_{3/2}$  signals indicate the near-surface Mn:Sb is approximately 1:1. The inset shows the Mn 3s signal from both films, where the larger peak

1  
2  
3 splitting in the Sb-Mn film is due to the presence of  $\text{Mn}^{+2}$ . (b) Using AP-XPS, Mn 2p spectra on  
4 the  $\text{Mn}_{0.70}\text{Sb}_{0.30}\text{O}_2$  sample reveals the presence of the  $\text{Mn}^{+2}$  satellite feature, indicating a mixture  
5 of  $\text{Mn}^{+2}$  and  $\text{Mn}^{+3}$  in the near surface. The intensity of the satellite feature is lower upon  
6 exposure to 0.2 Torr  $\text{H}_2\text{O}$  but still present, demonstrating oxidation resistance of the Sb-Mn film.  
7  
8  
9

#### 10 11 12 13 4. CONCLUSIONS 14 15

16 Stable oxygen evolution catalysis in strong acid electrolyte poses substantial challenges for non-  
17 precious metal electrocatalysts, with Mn oxide species able to provide substantial activity if  
18 incorporated in an environment that stabilizes  $\text{Mn}^{+3}$ . We show that such stabilization is provided  
19 by alloying Mn into a  $(\text{Sb},\text{Mn})\text{O}_2$  rutile structure, in particular with Mn-rich alloys that are  
20 reported here for the first time and supported by extensive DFT calculations including Pourbaix  
21 analysis that highlights the role of Sb and the rutile structure in stabilizing  $\text{Mn}^{+3}$  under OER  
22 conditions in acid. Characterization of the alloys by synchrotron x-ray absorption spectroscopy,  
23 which is supported by AP-XPS and computational analysis, reveals an increase in  $\text{Mn}^{+3}$   
24 concentration as well as Mn-O covalency with increasing Mn content in the alloy, both of which  
25 increase OER activity and make these manganese antimonates the most promising  
26 electrocatalysts for water electrolysis in acidic media without precious metals.  
27  
28  
29  
30  
31  
32  
33  
34  
35  
36  
37  
38  
39  
40  
41  
42

#### 43 ASSOCIATED CONTENT 44 45

##### 46 **Supporting Information** 47

48 The Supporting Information is available free of charge on the ACS Publications website at  
49 DOI:XXX.  
50

51  
52  
53 Experimental and computational details, additional electrochemical and materials  
54 characterization data.  
55  
56  
57

1  
2  
3 AUTHOR INFORMATION  
4  
5

6 **Corresponding Author**  
7

8 Kristin A. Persson (kapersson@lbl.gov), John M. Gregoire (gregoire@caltech.edu)  
9

10 **ORCID**  
11

12 Lan Zhou: 0000-0002-7052-266X  
13

14 Aniketa Shinde: 0000-0003-2386-3848  
15

16 Joseph H. Montoya: 0000-0001-5760-2860  
17

18 Arunima Singh:  
19

20 Sheraz Gul:  
21

22 Junko Yano:  
23

24 Yifan Ye:  
25

26 Ethan J. Crumlin:  
27

28 Matthias H. Richter:  
29

30 Jason K. Cooper:  
31

32 Helge S. Stein: 0000-0002-3461-0232  
33

34 Joel A. Haber: 0000-0001-7847-5506  
35

36 Kristin A. Persson: 0000-0003-2495-5509  
37

38 John M. Gregoire: 0000-0002-2863-5265  
39

40 **Notes**  
41

42 The authors declare no competing financial interest.  
43  
44

45 **ACKNOWLEDGMENT**  
46

47 This study is based upon work performed by the Joint Center for Artificial Photosynthesis, a  
48 DOE Energy Innovation Hub, supported through the Office of Science of the U.S. Department of  
49 Energy (Award No. DE-SC0004993). Computational work was additionally supported by the  
50 Energy (Award No. DE-SC0004993). Computational work was additionally supported by the  
51 Materials Project Program (Grant No. KC23MP) through the DOE Office of Basic Energy  
52  
53  
54  
55  
56  
57  
58  
59  
60



1  
2  
3 Sciences, Materials Sciences and Engineering Division, under Contract DE-AC02-05CH11231.  
4  
5 Computational resources were provided by the National Energy Research Scientific Computing  
6  
7 Center, a DOE Office of Science User Facility supported by the Office of Science of the DOE  
8  
9 under Contract No. DE-AC02-05CH11231. Part of this work (XAS data collection) was carried  
10  
11 out at Stanford Synchrotron Radiation Lightsource, SLAC National Accelerator Laboratory,  
12  
13 supported by the U.S. Department of Energy, Office of Science, Office of Basic Energy Sciences  
14  
15 under Contract No. DE-AC02-76SF00515. XAS studies were performed with support of the  
16  
17 Office of Science, OBES, Division of Chemical Sciences, Geosciences, and Biosciences (CSGB)  
18  
19 of the DOE under contract no. DE-AC02-05CH11231 (J.Y.). AP-XPS was carried out at  
20  
21 Advanced Light Source, Lawrence Berkeley National Laboratory, supported by the U.S.  
22  
23 Department of Energy, Office of Science, Office of Basic Energy Sciences under Contract No.  
24  
25 DE-AC02-05CH11231. We acknowledge support from the Beckman Institute of the California  
26  
27 Institute of Technology to the Molecular Materials Research Center that enabled vacuum XPS  
28  
29  
30  
31  
32  
33  
34  
35  
36  
37  
38  
39  
40  
41  
42  
43  
44  
45  
46  
47  
48  
49  
50  
51  
52  
53  
54  
55  
56  
57  
58  
59  
60

## REFERENCES

1. (a) McKone, J. R.; Lewis, N. S.; Gray, H. B., Will Solar-Driven Water-Splitting Devices See the Light of Day? *Chem. Mater.* **2014**, *26* (1), 407-414; (b) Reier, T.; Nong Hong, N.; Teschner, D.; Schlögl, R.; Strasser, P., Electrocatalytic Oxygen Evolution Reaction in Acidic Environments - Reaction Mechanisms and Catalysts. *Adv. Energy Mater.* **2016**, *7* (1), 1601275.
2. Walter, M. G.; Warren, E. L.; McKone, J. R.; Boettcher, S. W.; Mi, Q.; Santori, E. A.; Lewis, N. S., Solar Water Splitting Cells. *Chem. Rev.* **2010**, *110* (11), 6446-6473.
3. McCrory, C. C. L.; Jung, S.; Ferrer, I. M.; Chatman, S. M.; Peters, J. C.; Jaramillo, T. F., Benchmarking Hydrogen Evolving Reaction and Oxygen Evolving Reaction Electrocatalysts for Solar Water Splitting Devices. *J. Am. Chem. Soc.* **2015**, *137* (13), 4347-4357.
4. (a) Xiang, C.; Weber, A. Z.; Ardo, S.; Berger, A.; Chen, Y.; Coridan, R.; Fountaine, K. T.; Haussener, S.; Hu, S.; Liu, R.; Lewis, N. S.; Modestino, M. A.; Shaner, M. M.; Singh, M. R.; Stevens, J. C.; Sun, K.; Walczak, K., Modeling, Simulation, and Implementation of Solar-Driven Water-Splitting Devices. *Angew. Chem., Int. Ed.* **2016**, *55* (42), 12974-12988; (b) Jin, J.; Walczak, K.; Singh, M. R.; Karp, C.; Lewis, N. S.; Xiang, C., An experimental and modeling/simulation-based evaluation of the efficiency and operational performance characteristics of an integrated, membrane-free, neutral pH solar-driven water-splitting

- system. *Energy Environ. Sci.* **2014**, *7* (10), 3371-3380; (c) Singh, M. R.; Papadantonakis, K.; Xiang, C.; Lewis, N. S., An electrochemical engineering assessment of the operational conditions and constraints for solar-driven water-splitting systems at near-neutral pH. *Energy Environ. Sci.* **2015**, *8* (9), 2760-2767.
5. Kumari, S.; Ajayi, B. P.; Kumar, B.; Jasinski, J. B.; Sunkara, M. K.; Spurgeon, J. M., A low-noble-metal  $W_{1-x}Ir_xO_{3-\delta}$  water oxidation electrocatalyst for acidic media via rapid plasma synthesis *Energy Environ. Sci.* **2017**, *10* (11), 2432-2440.
6. Gaudet, J.; Tavares, A. C.; Trasatti, S.; Guay, D., Physicochemical Characterization of Mixed  $RuO_2$ - $SnO_2$  Solid Solutions. *Chem. Mater.* **2005**, *17* (6), 1570-1579.
7. Pérez-Viramontes, N. J.; Escalante-García, I. L.; Guzmán-Martínez, C.; Galván-Valencia, M.; Durón-Torres, S. M., Electrochemical study of Ir-Sn-Sb-O materials as catalyst-supports for the oxygen evolution reaction. *J. Appl. Electrochem.* **2015**, *45* (11), 1165-1173.
8. Kadakia, K.; Datta, M. K.; Velikokhatnyi, O. I.; Jampani, P.; Park, S. K.; Saha, P.; Poston, J. A.; Manivannan, A.; Kumta, P. N., Novel (Ir,Sn,Nb) $O_2$  anode electrocatalysts with reduced noble metal content for PEM based water electrolysis. *Int. J. Hydrogen Energy* **2012**, *37* (4), 3001-3013.
9. Sun, W.; Cao, L.-m.; Yang, J., Conversion of inert cryptomelane-type manganese oxide into a highly efficient oxygen evolution catalyst via limited Ir doping. *J. Mater. Chem. A* **2016**, *4* (32), 12561-12570.
10. Oakton, E.; Lebedev, D.; Povia, M.; Abbott, D. F.; Fabbri, E.; Fedorov, A.; Nachttegaal, M.; Copéret, C.; Schmidt, T. J.,  $IrO_2$ - $TiO_2$ : A High-Surface-Area, Active, and Stable Electrocatalyst for the Oxygen Evolution Reaction. *ACS Catal.* **2017**, *7* (4), 2346-2352.
11. Marshall, A. T.; Sunde, S.; Tsytkin, M.; Tunold, R., Performance of a PEM water electrolysis cell using  $Ir_xRu_yTa_zO_2$  electrocatalysts for the oxygen evolution electrode. *Int. J. Hydrogen Energy* **2007**, *32* (13), 2320-2324.
12. (a) Macounová, K.; Jirkovský, J.; Makarova, M. V.; Franc, J.; Krtil, P., Oxygen evolution on  $Ru_{1-x}Ni_xO_{2-y}$  nanocrystalline electrodes. *J. Solid State Electrochem.* **2009**, *13* (6), 959-965; (b) Reier, T.; Pawolek, Z.; Cherevko, S.; Bruns, M.; Jones, T.; Teschner, D.; Selve, S.; Bergmann, A.; Nong, H. N.; Schlögl, R.; Mayrhofer, K. J. J.; Strasser, P., Molecular Insight in Structure and Activity of Highly Efficient, Low-Ir Ir-Ni Oxide Catalysts for Electrochemical Water Splitting (OER). *J. Am. Chem. Soc.* **2015**, *137* (40), 13031-13040.
13. Tae, E. L.; Song, J.; Lee, A. R.; Kim, C. H.; Yoon, S.; Hwang, I. C.; Kim, M. G.; Yoon, K. B., Cobalt Oxide Electrode Doped with Iridium Oxide as Highly Efficient Water Oxidation Electrode. *ACS Catal.* **2015**, *5* (9), 5525-5529.
14. (a) Mondschein, J. S.; Callejas, J. F.; Read, C. G.; Chen, J. Y. C.; Holder, C. F.; Badding, C. K.; Schaak, R. E., Crystalline Cobalt Oxide Films for Sustained Electrocatalytic Oxygen Evolution under Strongly Acidic Conditions. *Chem. Mater.* **2017**, *29* (3), 950-957; (b) Blasco-Ahicart, M.; Soriano-López, J.; Carbó, J. J.; Poblet, J. M.; Galan-Mascaros, J. R., Polyoxometalate electrocatalysts based on earth-abundant metals for efficient water oxidation in acidic media. *Nat. Chem.* **2017**, *10*, 24; (c) Yang, X.; Li, H.; Lu, A.-Y.; Min, S.; Idriss, Z.; Hedhili, M. N.; Huang, K.-W.; Idriss, H.; Li, L.-J., Highly acid-durable carbon coated  $Co_3O_4$  nanoarrays as efficient oxygen evolution electrocatalysts. *Nano Energy* **2016**, *25*, 42-50; (d) Yan, K.-L.; Chi, J.-Q.; Xie, J.-Y.; Dong, B.; Liu, Z.-Z.; Gao, W.-K.; Lin, J.-H.; Chai, Y.-M.; Liu, C.-G., Mesoporous Ag-doped  $Co_3O_4$  nanowire arrays supported on FTO as efficient electrocatalysts for oxygen evolution reaction in acidic media. *Renewable Energy* **2018**, *119*, 54-61; (e) Yan, K.-L.; Qin, J.-F.; Lin, J.-H.; Dong, B.; Chi, J.-Q.; Liu, Z.-Z.; Dai, F.-N.; Chai, Y.-M.; Liu, C.-G., Probing the active sites of  $Co_3O_4$  for the acidic oxygen evolution reaction by modulating the  $Co^{2+}/Co^{3+}$  ratio. *J. Mater. Chem. A* **2018**, *6* (14), 5678-5686.
15. Kwong, W. L.; Lee, C. C.; Shchukarev, A.; Björn, E.; Messinger, J., High-performance iron (III) oxide electrocatalyst for water oxidation in strongly acidic media. *J. Catal.* **2018**, *365*, 29-35.

- 1  
2  
3 16. (a) Shinde, A.; Jones, R. J. R.; Guevarra, D.; Mitrovic, S.; Becerra-Stasiewicz, N.; Haber, J. A.; Jin,  
4 J.; Gregoire, J. M., High-Throughput Screening for Acid-Stable Oxygen Evolution Electrocatalysts in the  
5 (Mn-Co-Ta-Sb) $O_x$  Composition Space. *Electrocatalysis* **2015**, *6* (2), 229-236; (b) Huynh, M.; Ozel, T.; Liu,  
6 C.; Lau, E. C.; Nocera, D. G., Design of template-stabilized active and earth-abundant oxygen evolution  
7 catalysts in acid. *Chem. Sci.* **2017**, *8* (7), 4779-4794; (c) Patel, P. P.; Datta, M. K.; Velikokhatnyi, O. I.;  
8 Kuruba, R.; Damodaran, K.; Jampani, P.; Gattu, B.; Shanthi, P. M.; Damle, S. S.; Kumta, P. N., Noble  
9 metal-free bifunctional oxygen evolution and oxygen reduction acidic media electro-catalysts. *Sci. Rep.*  
10 **2016**, *6*, 28367; (d) Moreno-Hernandez, I. A.; MacFarland, C. A.; Read, C. G.; Papadantonakis, K. M.;  
11 Brunschwig, B. S.; Lewis, N. S., Crystalline nickel manganese antimonate as a stable water-oxidation  
12 catalyst in aqueous 1.0 M  $H_2SO_4$ . *Energy Environ. Sci.* **2017**, *10* (10), 2103-2108; (e) Frydendal, R.; Paoli,  
13 E. A.; Chorkendorff, I.; Rossmeisl, J.; Stephens, I. E. L., Toward an Active and Stable Catalyst for Oxygen  
14 Evolution in Acidic Media: Ti-Stabilized  $MnO_2$ . *Adv. Energy Mater.* **2015**, *5* (22), 1500991.
- 17 17. Post, J. E., Manganese oxide minerals: Crystal structures and economic and environmental  
18 significance. *Proc. Natl. Acad. Sci.* **1999**, *96* (7), 3447-3454.
- 19 18. Takashima, T.; Hashimoto, K.; Nakamura, R., Mechanisms of pH-Dependent Activity for Water  
20 Oxidation to Molecular Oxygen by  $MnO_2$  Electrocatalysts. *J. Am. Chem. Soc.* **2012**, *134* (3), 1519-1527.
- 21 19. Takashima, T.; Hashimoto, K.; Nakamura, R., Inhibition of Charge Disproportionation of  $MnO_2$   
22 Electrocatalysts for Efficient Water Oxidation under Neutral Conditions. *J. Am. Chem. Soc.* **2012**, *134*  
23 (44), 18153-18156.
- 24 20. (a) Zaharieva, I.; Chernev, P.; Risch, M.; Klingan, K.; Kohlhoff, M.; Fischer, A.; Dau, H.,  
25 Electrosynthesis, functional, and structural characterization of a water-oxidizing manganese oxide.  
26 *Energy Environ. Sci.* **2012**, *5* (5), 7081-7089; (b) Gorlin, Y.; Lassalle-Kaiser, B.; Benck, J. D.; Gul, S.; Webb,  
27 S. M.; Yachandra, V. K.; Yano, J.; Jaramillo, T. F., In Situ X-ray Absorption Spectroscopy Investigation of a  
28 Bifunctional Manganese Oxide Catalyst with High Activity for Electrochemical Water Oxidation and  
29 Oxygen Reduction. *J. Am. Chem. Soc.* **2013**, *135* (23), 8525-8534; (c) Huynh, M.; Shi, C.; Billinge, S. J. L.;  
30 Nocera, D. G., Nature of Activated Manganese Oxide for Oxygen Evolution. *J. Am. Chem. Soc.* **2015**, *137*  
31 (47), 14887-14904.
- 33 21. Morgan Chan, Z.; Kitchaev, D. A.; Nelson Weker, J.; Schnedermann, C.; Lim, K.; Ceder, G.; Tumas,  
34 W.; Toney, M. F.; Nocera, D. G., Electrochemical trapping of metastable  $Mn^{3+}$  ions for activation of  $MnO_2$   
35 oxygen evolution catalysts. *Proc. Natl. Acad. Sci.* **2018**, *115* (23), E5261-E5268.
- 37 22. Oh, H. S.; Nong Hong, N.; Strasser, P., Preparation of Mesoporous Sb-, F-, and In-Doped  $SnO_2$   
38 Bulk Powder with High Surface Area for Use as Catalyst Supports in Electrolytic Cells. *Adv. Funct. Mater.*  
39 **2015**, *25* (7), 1074-1081.
- 40 23. Seley, D.; Ayers, K.; Parkinson, B. A., Combinatorial Search for Improved Metal Oxide Oxygen  
41 Evolution Electrocatalysts in Acidic Electrolytes. *ACS Comb. Sci.* **2013**, *15* (2), 82-89.
- 42 24. Suram, S. K.; Zhou, L.; Becerra-Stasiewicz, N.; Kan, K.; Jones, R. J. R.; Kendrick, B. M.; Gregoire, J.  
43 M., Combinatorial thin film composition mapping using three dimensional deposition profiles. *Rev. Sci.*  
44 *Instrum.* **2015**, *86* (3), 033904.
- 46 25. Gregoire, J. M.; Xiang, C.; Liu, X.; Marcin, M.; Jin, J., Scanning droplet cell for high throughput  
47 electrochemical and photoelectrochemical measurements. *Rev. Sci. Instrum.* **2013**, *84* (2), 024102.
- 48 26. Jain, A.; Ong, S. P.; Hautier, G.; Chen, W.; Richards, W. D.; Dacek, S.; Cholia, S.; Gunter, D.;  
49 Skinner, D.; Ceder, G.; Persson, K. A., Commentary: The Materials Project: A materials genome approach  
50 to accelerating materials innovation. *APL Mater.* **2013**, *1* (1), 011002.
- 51 27. (a) Kresse, G.; Hafner, J., Ab initio molecular dynamics for liquid metals. *Phys. Rev. B* **1993**, *47*  
52 (1), 558-561; (b) Kresse, G.; Furthmüller, J., Efficiency of ab-initio total energy calculations for metals and  
53 semiconductors using a plane-wave basis set. *Comput. Mater. Sci.* **1996**, *6* (1), 15-50; (c) Kresse, G.;  
54 Furthmüller, J., Efficient iterative schemes for ab initio total-energy calculations using a plane-wave basis  
55  
56  
57  
58  
59  
60

- 1  
2  
3 set. *Phys. Rev. B* **1996**, *54* (16), 11169-11186; (d) Kresse, G.; Joubert, D., From ultrasoft pseudopotentials  
4 to the projector augmented-wave method. *Phys. Rev. B* **1999**, *59* (3), 1758-1775.
- 5 28. (a) Ong, S. P.; Richards, W. D.; Jain, A.; Hautier, G.; Kocher, M.; Cholia, S.; Gunter, D.; Chevrier, V.  
6 L.; Persson, K. A.; Ceder, G., Python Materials Genomics (pymatgen): A robust, open-source python  
7 library for materials analysis. *Comput. Mater. Sci.* **2013**, *68*, 314-319; (b) Singh, A. K.; Zhou, L.; Shinde, A.;  
8 Suram, S. K.; Montoya, J. H.; Winston, D.; Gregoire, J. M.; Persson, K. A., Electrochemical Stability of  
9 Metastable Materials. *Chem. Mater.* **2017**, *29* (23), 10159-10167.
- 10 29. Henkelman, G.; Arnaldsson, A.; Jónsson, H., A fast and robust algorithm for Bader  
11 decomposition of charge density. *Comput. Mater. Sci.* **2006**, *36* (3), 354-360.
- 12 30. Grass, M. E.; Karlsson, P. G.; Aksoy, F.; Lundqvist, M.; Wannberg, B.; Mun, B. S.; Hussain, Z.; Liu,  
13 Z., New ambient pressure photoemission endstation at Advanced Light Source beamline 9.3.2. *Rev. Sci.*  
14 *Instrum.* **2010**, *81* (5), 053106.
- 15 31. Manceau, A.; Marcus, M. A.; Grangeon, S., Determination of Mn valence states in mixed-valent  
16 manganates by XANES spectroscopy. *Am. Mineral.* **2012**, *97*, 816-827.
- 17 32. (a) Westin, G.; Grins, J., Rutile-Type  $Mn_{(1-x)}Sb_{(1+x)}O_4$  Phases,  $0 \leq x \leq 1/3$ , Synthesized by the Sol-  
18 Gel Technique. *Acta Chem. Scand.* **1993**, *47*, 1053-1056; (b) Westin, G.; Nygren, M., Sol-Gel Preparation  
19 of M-Sb oxides from  $Sb(OBu^n)_3$ -M-Acetate Precursors with M=Mn, Co, Ni. *J. Mater. Chem* **1993**, *3* (4),  
20 367-371.
- 21 33. Aykol, M.; Dwaraknath, S. S.; Sun, W.; Persson, K. A., Thermodynamic limit for synthesis of  
22 metastable inorganic materials. *Sci. Adv.* **2018**, *4* (4), eaaq0148.
- 23 34. Smith, D. C.; Perseil, E.-A., Sb-rich rutile in the manganese concentrations at St. Marcel-  
24 Praborna, Aosta Valley, Italy: petrology and crystal-chemistry. *Mineral. Mag.* **2018**, *61* (408), 655-669.
- 25 35. Biesinger, M. C.; Payne, B. P.; Grosvenor, A. P.; Lau, L. W. M.; Gerson, A. R.; Smart, R. S.,  
26 Resolving surface chemical states in XPS analysis of first row transition metals, oxides and hydroxides:  
27 Cr, Mn, Fe, Co and Ni. *Appl. Surf. Sci.* **2011**, *257* (7), 2717-2730.
- 28 36. (a) Robinson, D. M.; Go, Y. B.; Mui, M.; Gardner, G.; Zhang, Z.; Mastrogiovanni, D.; Garfunkel, E.;  
29 Li, J.; Greenblatt, M.; Dismukes, G. C., Photochemical Water Oxidation by Crystalline Polymorphs of  
30 Manganese Oxides: Structural Requirements for Catalysis. *J. Am. Chem. Soc.* **2013**, *135* (9), 3494-3501;  
31 (b) Smith, P. F.; Deibert, B. J.; Kaushik, S.; Gardner, G.; Hwang, S.; Wang, H.; Al-Sharab, J. F.; Garfunkel,  
32 E.; Fabris, L.; Li, J.; Dismukes, G. C., Coordination Geometry and Oxidation State Requirements of Corner-  
33 Sharing  $MnO_6$  Octahedra for Water Oxidation Catalysis: An Investigation of Manganite ( $\gamma$ - $MnOOH$ ). *ACS*  
34 *Catal.* **2016**, *6* (3), 2089-2099.
- 35 37. Seo, D.-H.; Lee, J.; Urban, A.; Malik, R.; Kang, S.; Ceder, G., The structural and chemical origin of  
36 the oxygen redox activity in layered and cation-disordered Li-excess cathode materials. *Nat. Chem.*  
37 **2016**, *8*, 692.
- 38 38. Grimaud, A.; Diaz-Morales, O.; Han, B.; Hong, W. T.; Lee, Y.-L.; Giordano, L.; Stoerzinger, K. A.;  
39 Koper, M. T. M.; Shao-Horn, Y., Activating lattice oxygen redox reactions in metal oxides to catalyze  
40 oxygen evolution. *Nat. Chem.* **2017**, *9*, 457.
- 41  
42  
43  
44  
45  
46  
47  
48  
49  
50  
51  
52  
53  
54  
55  
56  
57  
58  
59  
60

## TOC

